

Brillouin asymmetric spatial heterodyne oceanographic lidar receiver for profiling temperature, salinity, and sound velocity

*John A. Smith and Chris Hostetler
Langley Research Center, Hampton, Virginia*

NASA STI Program Report Series

Since its founding, NASA has been dedicated to the advancement of aeronautics and space science. The NASA scientific and technical information (STI) program plays a key part in helping NASA maintain this important role.

The NASA STI program operates under the auspices of the Agency Chief Information Officer. It collects, organizes, provides for archiving, and disseminates NASA's STI. The NASA STI program provides access to the NTRS Registered and its public interface, the NASA Technical Reports Server, thus providing one of the largest collections of aeronautical and space science STI in the world. Results are published in both non-NASA channels and by NASA in the NASA STI Report Series, which includes the following report types:

- **TECHNICAL PUBLICATION.** Reports of completed research or a major significant phase of research that present the results of NASA Programs and include extensive data or theoretical analysis. Includes compilations of significant scientific and technical data and information deemed to be of continuing reference value. NASA counterpart of peer-reviewed formal professional papers but has less stringent limitations on manuscript length and extent of graphic presentations.
- **TECHNICAL MEMORANDUM.** Scientific and technical findings that are preliminary or of specialized interest, e.g., quick release reports, working papers, and bibliographies that contain minimal annotation. Does not contain extensive analysis.
- **CONTRACTOR REPORT.** Scientific and technical findings by NASA-sponsored contractors and grantees.

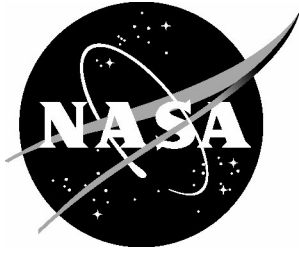
- **CONFERENCE PUBLICATION.** Collected papers from scientific and technical conferences, symposia, seminars, or other meetings sponsored or co-sponsored by NASA.
- **SPECIAL PUBLICATION.** Scientific, technical, or historical information from NASA programs, projects, and missions, often concerned with subjects having substantial public interest.
- **TECHNICAL TRANSLATION.** English-language translations of foreign scientific and technical material pertinent to NASA's mission.

Specialized services also include organizing and publishing research results, distributing specialized research announcements and feeds, providing information desk and personal search support, and enabling data exchange services.

For more information about the NASA STI program, see the following:

- Access the NASA STI program home page at <http://www.sti.nasa.gov>
- Help desk contact information: <https://www.sti.nasa.gov/sti-contact-form/> and select the "General" help request type.

NASA/TP–20240000673



Brillouin asymmetric spatial heterodyne oceanographic lidar receiver for profiling temperature, salinity, and sound velocity

*John A. Smith and Chris Hostetler
Langley Research Center, Hampton, Virginia*

National Aeronautics and
Space Administration

Langley Research Center
Hampton, Virginia 23681-2199

January 2024

The use of trademarks or names of manufacturers in this report is for accurate reporting and does not constitute an official endorsement, either expressed or implied, of such products or manufacturers by the National Aeronautics and Space Administration.

Available from:

NASA STI Program / Mail Stop 050
NASA Langley Research Center
Hampton, VA 23681-2199

1 **Brillouin asymmetric spatial heterodyne oceanographic lidar**
2 **receiver for profiling temperature, salinity, and sound velocity**

3 **JOHN A. SMITH AND CHRIS HOSTETLER**

4 *NASA Langley Research Center, Hampton, VA 23681, USA*

5 **john.a.smith-3@nasa.gov*

6 **Abstract:** A lidar receiver employing a proposed Brillouin asymmetric spatial
7 heterodyne (BASH) spectrometer to measure depth resolved profiles of near
8 surface ocean temperature, salinity, and sound velocity from aircraft is
9 conceptualized. A BASH spectrometer can have high throughput, can be
10 designed for any wavelength and, importantly, can be field widened, allowing
11 accurate, high spectral resolution of the Brillouin spectrum within diffuse
12 scatter from depth. Temperature and salinity are measured independently with
13 no assumptions about one or the other and the measurements are unbiased by
14 the presence of particulate or elastic scatter. A sensitivity analysis and lidar
15 simulations show the expected performance.

16 **1. Introduction**

17 No sensor today is capable of remotely sensing temperature and salinity at
18 depth. Existing techniques depend on infrared or microwave emissions that
19 originate from only the very surface (<1 mm) of the water, whereas lidars with
20 blue-green wavelength transmitters (450-550 nm) are capable of penetrating
21 10's of meters into the water. Light interacts with water by the Brillouin

22 (Brillouin-Mandelstam) scatter process, and by analyzing the spectrum of
23 Brillouin scatter from a water body the temperature and salinity can be
24 determined. For a pulsed laser source, temporally range gating the backscatter
25 signal can provide depth resolution. There are a host of scientific and
26 operational drivers for such a sensor, from improved hurricane and red tide
27 forecasting to studies of ocean fronts, eddies, and freshwater lenses. Though
28 the idea of using Brillouin scatter to measure physical properties of the ocean
29 has been around for several decades, no fieldable sensor has been demonstrated.
30 The challenge has been to spectrally resolve the features of the Brillouin
31 spectrum well enough in the diffuse backscatter from water to permit an
32 accurate and precise retrieval. A variety of methods have been explored by
33 several groups to accomplish this. They include the use Faraday anomalous
34 dispersion optical filters [1], Fabry-Perot interferometers [2-6], and iodine and
35 barium vapor cells [4,7]. Vapor cells can achieve a large etendue, but they do
36 not fully resolve the Brillouin spectrum. The Fabry-Perot interferometer and
37 close cousin, the virtually imaged phased array (VIPA), resolves the spectrum
38 well enough to determine both the Brillouin shift and linewidth, and therefore
39 both temperature and salinity, but have a very limited etendue. Approaches
40 have been studied that exploit the temperature and salinity dependence of the
41 spectrum of Raman scatter, but their measurement performance is inherently
42 limited during daytime due to the large spectral bandwidth of the Raman return
43 (30-40 nm). A rugged and fieldable Brillouin lidar sensor concept is presented

44 here that combines the etendue advantages of atomic and molecular vapor
45 filters with the spectral resolution advantage of interferometric approaches,
46 overcoming a major limitation of existing approaches.

47 A variation on the original Doppler asymmetric spatial heterodyne (DASH)
48 technique – here referred to as the Brillouin asymmetric spatial heterodyne
49 (“BASH”) technique – is presented. The original, Doppler variant has been used
50 to resolve Doppler shifts in airglow to measure winds in the upper atmosphere
51 [8,9]. Spatial heterodyne techniques have not previously been prescribed for
52 use in a Brillouin lidar, to this author’s knowledge, but do have advantages for
53 this application. For example, the BASH technique can be implemented using
54 field widened (or field “compensated”) interferometers. Since scatter from
55 depths in the ocean is diffuse, like airglow, this is a distinct advantage. The
56 BASH technique also provides enough spectral information to infer Brillouin
57 shift, Brillouin linewidth and the presence of elastic scatter unambiguously,
58 without requiring assumptions on any of these three variables. The polarizing
59 BASH variant presented here can offer very high light throughput and can be
60 designed for any wavelength that efficiently penetrates water. Spatial
61 heterodyne interferometers are also rugged and have heritage with other
62 instruments. For example, a DASH called MIGHTI flew on NASA’s ICON
63 spacecraft [10], and a Michelson interferometer that shares structural
64 similarities to the DASH has flown in the 355 nm receiver channel of NASA
65 Langley Research Center’s HSRL-2 airborne high spectral resolution lidar to

66 make high spectral resolution measurements of aerosols and clouds on many
67 campaigns focused on atmospheric science [11-14].

68 **2. Description of BASH technique and application to resolving Brillouin** 69 **spectrum**

70 Here, we describe the use of the novel polarizing BASH technique for resolving
71 the spectrum of Brillouin backscatter to determine the temperature, salinity, and
72 sound velocity within a water volume. The polarizing BASH technique is
73 implemented using an interferometer that is a close cousin of the polarizing
74 Michelson interferometer, but with the end mirrors replaced with gratings tilted
75 near Littrow (Fig. 1). The tilted gratings provide a spatial representation of the
76 Fourier transform of the input spectrum at the output, much like a monolithic
77 Fourier transform spectrometer. This polarizing interferometer does not reflect
78 light back to the source, and therefore has twice the throughput of a non-
79 polarizing interferometer. The polarizing DASH was introduced in [15], and
80 the polarizing BASH inherits from this design.

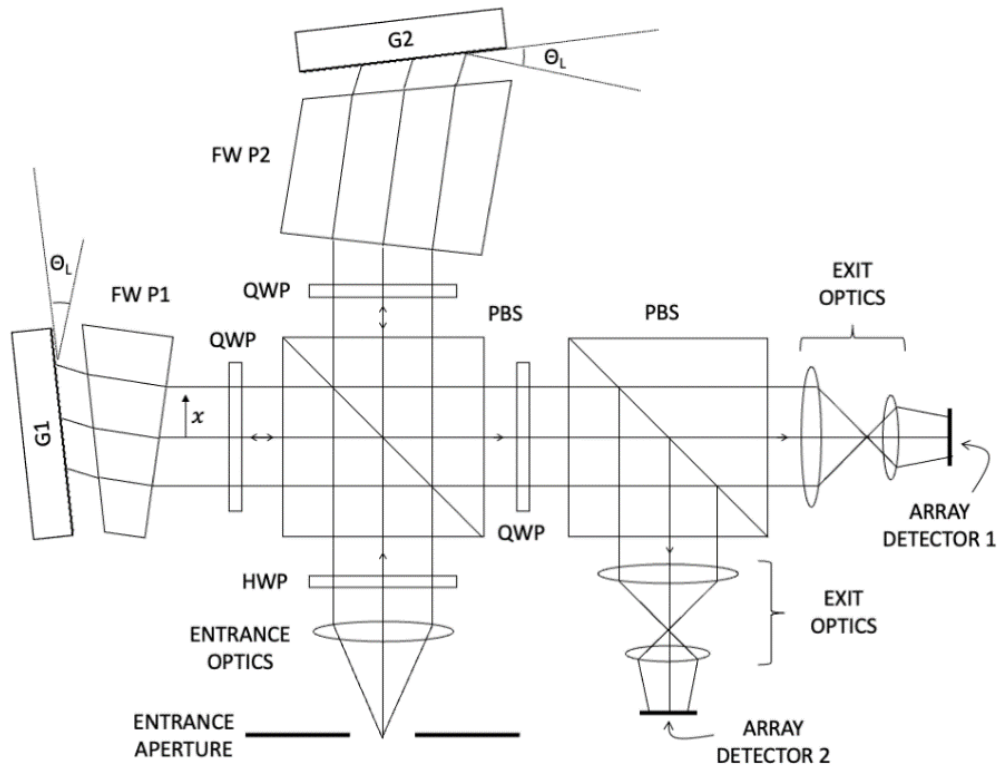


Fig. 1. Illustration of dual output polarizing interferometer implementing BASH technique. HWP: half waveplate, QWP: quarter waveplate, PBS: polarizing beam splitter, FW P1 and FW P2: field widening prisms, G1 and G2: gratings.

Light entering the entrance aperture is linearly polarized in the vertical direction. After passing through the half waveplate, the polarization is rotated 45 degrees such that the subsequent polarizing beam splitter provides a 50:50 split. The light in each arm passes through field widening prisms that reduce the sensitivity of the optical path difference (OPD) between the arms to the off-axis angle, thereby enhancing the field of view. The gratings are tilted at near

92 the Littrow angle to create a resolvable spatial heterodyne across an OPD range
 93 spanning many wavelengths (10^4 - 10^5). Upon passing twice through the quarter
 94 waveplate, the polarization is rotated 90 degrees from its original orientation
 95 and the light is directed toward the second polarizing beam splitter without
 96 returning towards the source. A quarter waveplate between the first and second
 97 polarizing beam splitters is oriented such that the two polarizations from each
 98 arm interfere. Having experienced a change in phase from a difference in the
 99 optical paths between the two arms, the interfered beams have a new linear
 100 polarization with a rotation that depends on the precise phase difference
 101 between them. Changes in polarization rotation are detected as changes in the
 102 split ratio of the second polarizing beam splitter. The second polarizing beam
 103 splitter therefore creates two, complementary interferograms. Each
 104 interferogram is imaged onto its respective array detector. For light entering the
 105 entrance aperture with a spectral distribution $f(\nu)$, the background-subtracted
 106 interferograms acquired by the two array detectors can be modeled as follows.

$$\begin{aligned}
 I_1(x) &= \eta_1 E_0 \frac{a_1}{2} \left(1 \right. \\
 &\quad \left. + M_1 \int_0^\infty f(\nu) \cos(2\pi(\nu - \nu_L)(4x \tan \theta_L + 2\Delta d)/c) d\nu \right)
 \end{aligned} \tag{1}$$

$$\begin{aligned}
I_2(x) &= \eta_2 E_0 \frac{a_2}{2} \left(1 \right. \\
&\quad \left. - M_2 \int_0^\infty f(\nu) \cos(2\pi(\nu - \nu_L)(4x \tan \theta_L + 2\Delta d)/c) d\nu \right)
\end{aligned} \tag{2}$$

107 Coefficients a_1 , a_2 , M_1 and M_2 parameterize defects in the interferometer
 108 and are unity for a perfect interferometer with a well collimated input (field
 109 widening will be treated later). M_1 and M_2 are referred to here as “visibility
 110 factors.” η_1 and η_2 are the photon detection efficiencies of the array detectors
 111 and E_0 is proportional to the input irradiance. x is a linear position along the
 112 grating aperture in the plane of Fig. 1, which maps to a linear position along the
 113 detector arrays, with $x = 0$ being the center. The factor $4x \tan \theta_L + 2\Delta d$ is the
 114 OPD and ν_L is the Littrow frequency. The spectral distribution of the input is
 115 approximated as a convolution of the laser transmitter spectrum (f_l) centered
 116 on its carrier frequency (ν_0) with a pair of Lorentz (Cauchy) distributions
 117 centered about $\nu_0 + \nu_B$ and $\nu_0 - \nu_B$ representing the Brillouin doublet plus a
 118 central Dirac delta function at ν_0 representing the residual elastic scatter, as
 119 shown in Eq. (3). γ is the ratio of elastic scatter to Brillouin scatter incident on
 120 the BASH and ν_B and Γ_B are the Brillouin shift and linewidth (FWHM),
 121 respectively.

$$f(\nu) = f_l(\nu - \nu_0) \otimes \left\{ \frac{1}{1 + \gamma} \frac{1}{\pi \Gamma_B} \left[\frac{1}{1 + \left(\frac{\nu - \nu_0 + \nu_B}{\Gamma_B/2} \right)^2} + \frac{1}{1 + \left(\frac{\nu - \nu_0 - \nu_B}{\Gamma_B/2} \right)^2} \right] + \frac{\gamma}{1 + \gamma} \delta_\nu(\nu - \nu_0) \right\} \quad (3)$$

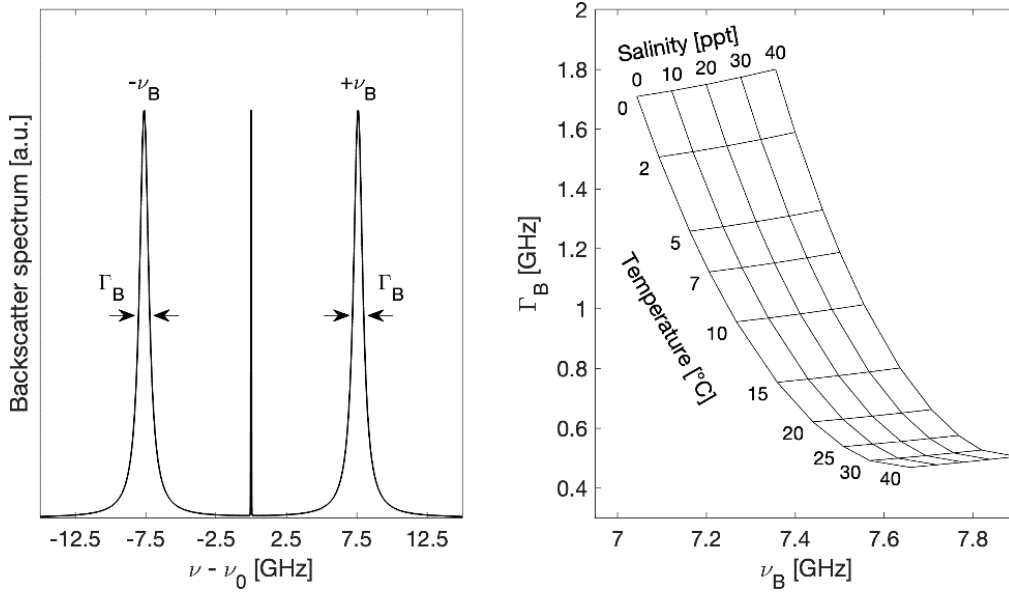
122 The Brillouin shift and Brillouin linewidth relate to the optical and physical
 123 properties of the water by Eq. (4) and Eq. (5), which pertain to a backscatter
 124 geometry.

$$\nu_B = \frac{2}{\lambda/n_{sw}} V_S \quad (4)$$

$$\Gamma_B \cong 8\pi \left(\frac{1}{\lambda/n_{sw}} \right)^2 \frac{1}{\rho} \left(\frac{4}{3} \eta_s + \eta_b \right) \quad (5)$$

125 Rayleigh scatter is ignored here, as it has a very small cross section
 126 compared to Brillouin scatter. Also ignored is a very small dependence on
 127 pressure. Note that the index of refraction of seawater (n_{sw}), sound velocity
 128 (V_S), bulk viscosity (η_b), shear viscosity (η_s) and density (ρ) are all temperature
 129 and salinity dependent. In this work, the index of refraction of seawater derives
 130 from [16], the sound velocity and seawater density derive from [17], the bulk
 131 viscosity derives from [18], and the shear (dynamic) viscosity derives from
 132 [19]. There is an additional term in Eq. (5) that depends on the thermal
 133 conductivity and the specific heats at constant volume and constant pressure,

134 but it is about two orders of magnitude smaller than the terms that depend on
 135 the bulk and shear viscosities and so is omitted here. By these sources and Eq.
 136 (4) and Eq. (5), the Brillouin shift and linewidth map to a unique temperature
 137 and salinity (Fig. 2). Ppt indicates parts per thousand or g/kg (‰).



138

139 Fig. 2. Illustration of Brillouin doublet centered on elastic scatter
 140 peak (left) and mapping of Brillouin shift and FWHM linewidth
 141 to temperature and salinity (right) for 532 nm illumination.

142 Making the convenient substitutions $4x \tan \theta_L + 2\Delta d \rightarrow \delta$, δ now referring
 143 to the optical path difference (OPD), and $\nu \rightarrow \nu' + \nu_0$, then inserting Eq. (3)
 144 into Eqs. (1) and (2) and performing the integration over ν' , the results are

$$I_1(\delta) = \eta_1 N_A \frac{a_1}{2} \left(1 \right. \quad (6)$$

$$+ M_1'(\delta) \left(\frac{1}{1+\gamma} \exp\left(-\frac{\pi\Gamma_B\delta}{c}\right) \cos\left(\frac{2\pi\nu_B\delta}{c}\right) \right. \\ \left. \left. + \frac{\gamma}{1+\gamma} \right) \cos\left(\frac{2\pi(\nu_L - \nu_0)\delta}{c}\right) \right)$$

$$I_2(\delta) = \eta_2 N_A \frac{a_2}{2} \left(1 \right. \quad (7)$$

$$- M_2'(\delta) \left(\frac{1}{1+\gamma} \exp\left(-\frac{\pi\Gamma_B\delta}{c}\right) \cos\left(\frac{2\pi\nu_B\delta}{c}\right) \right. \\ \left. \left. + \frac{\gamma}{1+\gamma} \right) \cos\left(\frac{2\pi(\nu_L - \nu_0)\delta}{c}\right) \right)$$

145 $M_1'(\delta)$ and $M_2'(\delta)$ are the visibility factors modified by the effects of a
 146 transmitter with a non-zero spectral width. The last cosine factor is a heterodyne
 147 between the Littrow frequency and the laser's carrier frequency and has a
 148 spatial period of $c/|\nu_L - \nu_0|$. Critically, the Brillouin shift and Brillouin
 149 linewidth information is encoded in the amplitude "envelope" of this Littrow
 150 heterodyne, as shown in Fig. 3. This contrasts with the traditional DASH
 151 technique in which the information (i.e., Doppler shift) is encoded in the phase
 152 of the Littrow heterodyne rather than its amplitude.

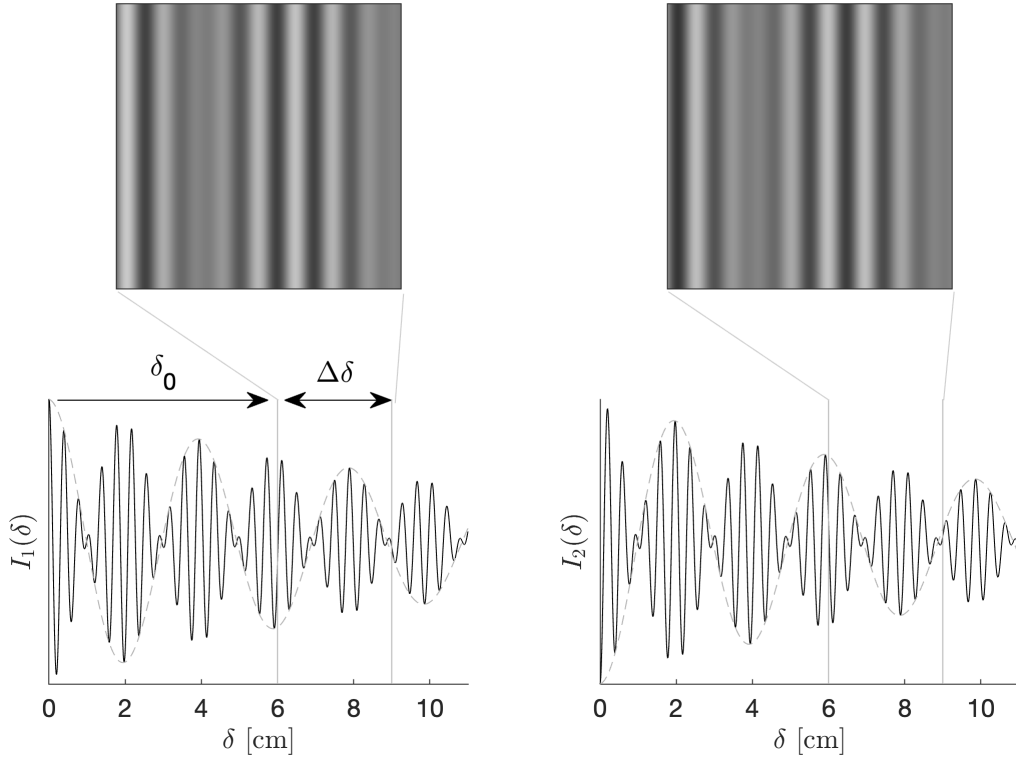


Fig. 3. Noiseless representations of the interferograms imaged by the two array detectors (top) and cross-sections of those interferograms (bottom). An OPD (δ) from δ_0 (6 cm) to $\delta_0 + \Delta\delta$ (9 cm) is illuminated in this example. The amplitude of the Littrow heterodyne envelope decays exponentially with the OPD according to the Brillouin linewidth and oscillates with a spatial frequency that depends on the Brillouin shift.

After acquiring the two interferograms, a ratio of the interferograms, what will be referred to here as the “normalized interferogram,” is formed to isolate the terms that depend only on the Brillouin shift (ν_B), Brillouin linewidth (Γ_B),

164 ratio of elastic to inelastic scatter (γ), and Littrow heterodyne frequency ($\nu_L -$
 165 ν_0).

$$\begin{aligned}
 Q(\delta) &= \frac{I_1(\delta) - \left(\frac{\eta_1 a_1}{\eta_2 a_2}\right) I_2(\delta)}{M_2'(\delta) I_1(\delta) + M_1'(\delta) \left(\frac{\eta_1 a_1}{\eta_2 a_2}\right) I_2(\delta)} \quad (8) \\
 &= \left[\frac{1}{1 + \gamma} \exp(-\pi \Gamma_B \delta / c) \cos(2\pi \nu_B \delta / c) \right. \\
 &\quad \left. + \frac{\gamma}{1 + \gamma} \right] \cos(2\pi(\nu_L - \nu_0) \delta / c)
 \end{aligned}$$

166 $(\eta_1 a_1)/(\eta_2 a_2)$ is referred to here as the “gain ratio” and can be obtained by
 167 taking the ratio of the interferograms averaged over the spatial period of the
 168 Littrow heterodyne, or, ideally, by observing a white light source like solar
 169 background. $M_1'(\delta)$ and $M_2'(\delta)$ can be determined using scatter from the water
 170 surface, or by episodically injecting a narrowband source. The Littrow
 171 heterodyne period can be continually assessed using any available Brillouin or
 172 elastic scatter.

173 From Eq. (8), the OPD offset that will maximize the sensitivity of the
 174 amplitude and phase of the envelope to both Brillouin linewidth and shift,
 175 respectively, is $\delta \cong c/(\pi \Gamma_B)$. For an OPD that falls within the optimum range
 176 for water temperatures between 0 and 35 °C and a transmitter with a 10 ns pulse
 177 width or greater and transform limited spectral width, the factors $M_1'(\delta)$ and
 178 $M_2'(\delta)$ are vanishingly close to M_1 and M_2 , respectively. M_1 and M_2 may still
 179 exhibit a dependence on OPD from imperfections, however.

180 **3. Temperature, salinity, and sound velocity error sensitivities**

181 What has been discussed up to this point is the average behavior of the
182 normalized interferogram and its dependence on the Brillouin shift and
183 linewidth. However, the interferograms, once acquired, will have detection
184 noise. The attention now turns to estimating the random errors in the retrievals
185 of Brillouin shift and linewidth caused by detection noise, with further
186 propagation to random uncertainties in temperature, salinity, and sound
187 velocity. The process for determining the variance of the normalized
188 interferogram on account of detection noise on the interferograms, as shown in
189 Appendix A, derives from another work [20] in which the analogous case of a
190 fringe imaged, tilted Mach-Zehnder was studied. A model is fitted to the
191 normalized interferogram to estimate the Brillouin shift, linewidth and elastic
192 scatter ratio parameters, so the Jacobian of the normalized interferogram can be
193 used to obtain the variance and covariance of the parameters, as shown in
194 Appendix B. A second Jacobian describing the sensitivities of the Brillouin
195 shift and linewidth parameters to temperature and salinity can then be used to
196 transform the parameter covariance matrix into a covariance matrix of
197 temperature and salinity, and another transform can be used to convert the
198 covariance matrix of the temperature and salinity to variance in sound velocity,
199 as shown in Appendix C. Only the results are shown in this section.

200 Estimating uncertainties in temperature, salinity, and sound velocity requires
201 knowing the sensitivities of the Brillouin shift and Brillouin linewidth to

202 temperature and salinity, and the sensitivity of sound velocity to temperature
 203 and salinity. Examples of these sensitivities for three water temperatures, a
 204 salinity of 35 ppt and 532 nm illumination are provided in Table 1. The sound
 205 velocity and its sensitivities derive from [17].

206 **Table 1. Sensitivities of the Brillouin shift and linewidth and sound**
 207 **velocity to temperature and salinity.**

		5 °C	15 °C	25 °C
$\partial v_B / \partial T$	MHz/°C	20.2	15.4	11.5
$\partial \Gamma_B / \partial T$		-76.1	-34.0	-13.1
$\partial v_B / \partial S$	MHz/ppt	7.52	6.94	6.49
$\partial \Gamma_B / \partial S$		2.05	1.33	1.02
$\partial V_s / \partial T$	m/s/°C	4.06	3.16	2.41
$\partial V_s / \partial S$	m/s/ppt	1.28	1.17	1.08

208

209 A numerical example is provided to check the accuracy of results from the
 210 analytical expressions derived in Appendices A through C against a Monte
 211 Carlo scheme. The parameters in Table 2 are assumed for the numerical
 212 example and will also be assumed for the lidar simulations later. The
 213 uncertainties pertain to a salinity of 35 ppt and 532 nm illumination. Also, the
 214 pixel density is assumed to be large compared to the Littrow heterodyne

215 wavenumber (i.e., $P/\Delta\delta \gg |\nu_L - \nu_0|/c$), and the pixels are assumed to be large
 216 enough that the covariance (i.e., optical crosstalk) between neighboring pixels
 217 can be neglected.

218 **Table 2. Parameters assumed for the calculation of uncertainties.**

γ	0.1
$ \nu_L - \nu_0 $	76.1 GHz
$\Delta\delta$	3 cm
δ_0	6 cm
F_B	-1
M_i	0.8

219
 220 The Monte Carlo random error estimates are obtained by creating Poisson
 221 random realizations of the two interferograms, computing the normalized
 222 interferogram, applying a least-squares fit to obtain the Brillouin shift and
 223 linewidth, then solving iteratively for temperature and salinity using Eq. (C 1).
 224 The process is repeated 1,000 times to obtain statistics. The sound velocity is
 225 then computed for each retrieved set of temperature and salinity. The standard
 226 deviations of the retrieved temperature, salinity, and sound velocity across
 227 iterations are computed and then normalized to SNR [Eq. (A 8)] to derive the

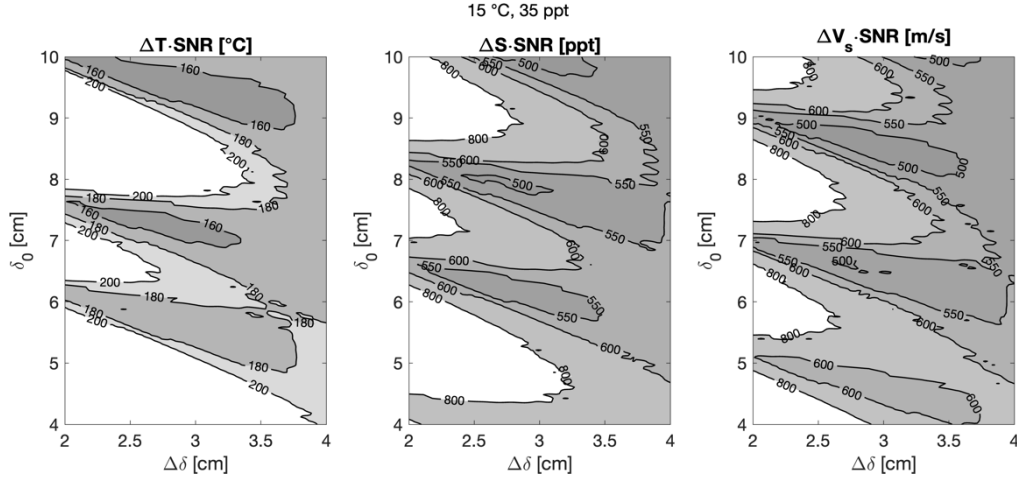
inverse sensitivity. Results for a range of temperatures and salinities are shown in Table 3 alongside the corresponding analytical result.

Table 3. Comparisons of estimates of inverse sensitivity in temperature, salinity, and sound velocity for the analytical and Monte Carlo methods for a range of temperatures and salinities typical of natural water bodies. The inverse sensitivities are divided by the SNR to obtain the random error in the corresponding quantity.

		0 °C		15 °C		30 °C	
		0 ppt	35 ppt	0 ppt	35 ppt	0 ppt	35 ppt
ΔT	Analytical	108	120	170	183	644	667
$\cdot SNR$ [°C]	Monte Carlo	110	127	167	200	553	710
ΔS	Analytical	1,207	1,069	587	532	1,042	1,022
$\cdot SNR$ [ppt]	Monte Carlo	1,253	1,125	599	560	935	1,064
ΔV_s	Analytical	1,628	1,582	669	608	606	561
$\cdot SNR$ [m/s]	Monte Carlo	1,632	1,616	697	605	586	585

The agreement between the analytical and Monte Carlo method results in Table 3 across temperature and salinity provides confidence in the accuracy of the analytical model results. The contour plots in Fig. 4 show the 1σ random error maps for an SNR of unity across OPD range ($\Delta\delta$) and offset (δ_0) for

240 temperature (ΔT), salinity (ΔS) and sound velocity (ΔV_s) estimated by the
 241 analytical method.



242
 243 Fig. 4. Contour plots of 1σ random error in temperature, salinity,
 244 and sound velocity (left to right) for an SNR of unity, water
 245 temperature of 15 °C and a salinity of 35 ppt across OPD range
 246 (horizontal axis) and OPD offset (vertical axis).

247 Fig. 4 can be used to select an optimum OPD range and OPD offset for the
 248 target application. Once an OPD offset and range are selected, the sensitivities
 249 to temperature, salinity, and sound velocity can be derived using the process
 250 outlined above and combined with SNR from lidar simulations to estimate the
 251 random errors for each quantity. The sections that follow are dedicated to
 252 deriving this SNR.

253 To compare the sensitivities of Brillouin spectrometers, it is sometimes
 254 instructive to express the Brillouin shift random error in terms of a multiple (α)

255 of the Brillouin linewidth divided by the SNR (i.e., $\Delta\nu_B = \alpha\Gamma_B/SNR$), as some
256 authors, e.g. [2,7], have done. A BASH with an OPD offset of 6 cm and an OPD
257 range of 3 cm and no defects achieves an α of between 3.1-3.3 from 5 °C to 25
258 °C when elastic scatter is negligible compared to Brillouin scatter.

259 **4. Discussion on operating altitude, field of view and collection area**

260 After determining OPD range and OPD offset, the next design choice is the
261 operating altitude and telescope size. It is desirable to have a receiver footprint
262 size of at least 6 m on the ocean surface for near-coastal water types [21]. A
263 footprint of this size will allow efficient collection of multiple scatter from
264 depth, making the apparent attenuation of the beam with depth closer to what's
265 referred to as the *diffuse attenuation coefficient*. Receivers with narrower fields
266 of view and limited multiple scatter collection result in attenuation that is closer
267 to the *beam attenuation coefficient*, which is much higher than the diffuse
268 attenuation coefficient, and even more so for productive, coastal water types.
269 For example, for waters with a chlorophyll concentration of 1 mg/m³, the
270 diffuse attenuation is about 0.1 /m whereas the beam attenuation is 0.25-0.4 /m.
271 Therefore, an apparent attenuation closer to beam attenuation would, for the
272 same SNR, provide 2.5-4 times less penetration. For a field of view that
273 provides a 6 m receiver footprint on the ground, the amount of scatter collected
274 will scale directly with the acceptance etendue ($A\Omega$) of the receiver, so it is
275 desirable for an ocean lidar receiver to accommodate a large etendue.

276 A larger field of view will also allow diverging the transmit beam such that
277 the energy density at the surface is below levels that would be harmful to
278 humans or marine life. A 2 m dia. $(1/e^2)$ Gaussian beam with a 2 mJ energy has
279 a peak energy density of $1.3 \cdot 10^{-7}$ J/cm², which is below the maximum
280 permissible exposure (MPE) for a 10 ns, 532 nm laser pulse. At a pulse
281 repetition rate of 4 kHz, the average power density is $5.2 \cdot 10^{-4}$ W/cm², which is
282 below the MPE for all exposure durations. A large etendue therefore also has
283 advantages for eye safety.

284 For most receivers, the etendue of the highest spectral resolution optic will
285 govern the etendue of the receiver. The Brillouin spectrometer will likely be the
286 highest spectral resolution optic in this application. An advantage of
287 spectrometers employing the BASH technique is that they can be (and often
288 are) field widened. Field widening is achieved by introducing refractive
289 elements in the arms of the interferometer to create a ‘quasi-zero’ path
290 difference condition in which the rays from each arm emerge mostly parallel
291 and coincident with each other while still having experienced a non-zero optical
292 path difference. This has the effect of enhancing the field of view and etendue
293 of the interferometer. In the case of the BASH, field widening is accomplished
294 by inserting a prism in each arm. The case of prisms with an index of refraction
295 greater than two will be assumed here. The ray tracing algebra was worked out
296 in [22] for this case, which finds the quartic angular dependence of the OPD
297 shown in Eq. (9).

$$\delta(\vartheta) \approx \delta(0) + \frac{\delta(0)}{16n^2}\vartheta^4 \quad (9)$$

298 $\delta(0)$ is the OPD for a ray at normal incidence, ϑ is the off-axis angle and n
 299 is the index of refraction of the prisms. The impact to the visibility factors M_1
 300 and M_2 can be assessed by integrating the cosine of the phase deviation caused
 301 by the OPD deviation $\delta(\vartheta) - \delta_0$ over the distribution of ray angles $f(\theta)$, i.e.

$$M_\Omega = \int_{\Omega} f(\vartheta) \cos(2\pi(\delta(\vartheta) - \delta(0))/\lambda) d\Omega \quad (10)$$

302 Assume a uniform, circular distribution of ray angles that extend up to a half
 303 angle of θ_M . The etendue-limited visibility factor is then, after series expansion

$$M_\Omega \approx 1 - \frac{\pi^2}{640n^4} \left(\frac{\delta_0}{\lambda}\right)^2 \theta_M^8 \quad (11)$$

304 M_1 and M_2 are both degraded by the factor M_Ω , but note the 8th order
 305 dependence on divergence. For water-clear ZnS prisms with an index of
 306 refraction of 2.40 at 532 nm and an OPD offset of 9 cm, >99.9% of the visibility
 307 can be preserved by limiting the incident ray angle divergence to a half angle
 308 of 50 mrad. If the interferometer's aperture is 2.5 cm \times 2.5 cm, the aircraft's
 309 altitude is 300 m, and the receiver's full angle field of view is 6 m/300 m \sim 20
 310 mrad, the telescope's collection area can be as large as 12.5 cm \times 12.5 cm (156
 311 cm²) while still satisfying the above angular limits. A 156 cm² collection area
 312 and 300 m flying altitude will be assumed in the simulations later in this work.
 313 It should be noted that the ZEMAX ray trace model for this same case [22]

314 showed higher angular sensitivity than that predicted by Eq. (9), which used
 315 small angle approximations. A more detailed study with ray tracing software is
 316 warranted.

317 To illustrate the value of field widening for this application, consider a
 318 comparison with the Fabry-Perot interferometer (FPI) and virtually imaged
 319 phased array (VIPA) that have previously been studied for use in Brillouin
 320 spectroscopy [23-27]. For a shift of half a fringe across the solid angle of
 321 acceptance, the limiting etendues [22] for receivers employing an FPI/VIPA
 322 and BASH are

$$(A\Omega)_{FPI/VIPA} = A \frac{2\pi}{R} \quad (12)$$

$$(A\Omega)_{BASH} = A \frac{2\sqrt{2}\pi}{\sqrt{R}} n \quad (13)$$

323 Where R is the interferometer's resolving power and A is the area of its
 324 useable aperture. The resolving power for the BASH specified in Section 3 is
 325 $\delta/\lambda \sim 10^5$. The limiting etendue for an FPI with the same aperture and
 326 resolving power, by Eqs. (12) and (13), would be approximately 1,000 times
 327 less than that of the BASH. An FPI and VIPA with equal resolving power will
 328 have a similar solid angle of acceptance, but the VIPA has the additional
 329 constraint of requiring that the input light pass through a narrow effective
 330 entrance slit to get past the edge of a high reflection coating, greatly limiting its
 331 useable aperture [28]. The BASH therefore collects at least 1,000 times more

332 scatter and will achieve at least $\sqrt{1000} \approx 32$ times higher SNR than an FPI or
333 VIPA for this wide field of view, eye safe lidar. Accurate measurements of the
334 Brillouin shift or linewidth by the FPI or VIPA may also be confounded by
335 changes in the diffuseness of the scatter with depth.

336 **5. Random errors in temperature, salinity, and sound velocity**

337 The parameters in Table 4 will be assumed for the lidar simulations. The aircraft
338 will be assumed to fly at an altitude of 300 m and at a speed of 130 m/s (250
339 kts). The laser transmitter parameters are borrowed from NASA Langley
340 Research Center's HSRL-1 airborne high spectral resolution lidar [29]. The
341 photon detection efficiency and excess noise factor figures are consistent with
342 commercial intensified cameras with a filmless MCP, GaAsP photocathode and
343 fast (ns) gating function. A thin film interference filter suppresses solar
344 background, limiting the effective passband to 0.5 nm. A polarizing element
345 directs the depolarized component of the backscatter to another detector. Since
346 the Brillouin backscatter is mostly copolarized with the transmitter and the solar
347 background is mostly depolarized, the polarizer affords a further factor of ~two
348 reduction in solar background while efficiently transmitting the Brillouin
349 scatter. It should be noted that, by Eqs. (B 3) and (B 4), the sensitivity to
350 Brillouin shift and linewidth will decrease when elastic scatter is present, and
351 elastic scatter may be ~10 times stronger than Brillouin scatter for more
352 productive waters. To mitigate the impact of elastic scatter on the sensitivity,

353 the backscatter will transmit through an iodine cell before the BASH and the
354 laser transmitter will be tuned to an absorption feature of iodine that suppresses
355 elastic scatter and efficiently passes the Brillouin scatter, as is done in HSRL-1
356 to implement the high spectral resolution lidar technique [29]. A functionally
357 similar alternative to the iodine cell would be a field widened Michelson with
358 a free spectral range of twice the Brillouin shift [30], and this approach would
359 not be limited to wavelengths that correspond to absorption lines.

360 **Table 4. Lidar instrument parameters assumed for the simulations.**

E_p	Energy per pulse	2 mJ
PRF	Pulse repetition frequency	4 kHz
λ	Wavelength	532 nm
η_t	Transmit optics efficiency	90%
η_r	Receiver optics efficiency	50%
A	Receiver collection area	156 cm ²
FOV	Receiver field of view, full angle	20 mrad
L	Lidar altitude	300 m
$\Delta\lambda$	Receiver effective passband	0.5 nm
η	Photon detection efficiency	50%
F	Excess noise factor, power space	2.6

361

362 The geophysical variables in Table 5 will be assumed for these simulations.

363 The apparent attenuation is assumed to be constant with depth and equal to the

364 diffuse attenuation coefficient. The depolarization ratio is also assumed to be

365 constant with depth.

366 **Table 5. Geophysical parameters assumed for the simulations. Mm is**

367 **megameter (10^6 m).**

T_a	One-way atmospheric transmittance	95%
T_s	One-way surface transmittance	98%
K_d	Diffuse attenuation coefficient	0.1 /m
β_{sw}	Seawater backscatter coefficient	0.232 /Mm/sr
δ_{sw}	Seawater depolarization ratio	0.039
n_{sw}	Seawater index of refraction	1.34
$L_{e,\Omega,\lambda}$	Upwelling solar radiance	7.5 mW/m ² /sr/nm

368

369 The following equations describe the number of Brillouin backscatter (N_A)

370 and solar background (N_B) photons received from a range bin with a vertical

371 extent (depth resolution) of Δz at a depth of z after integrating M laser shots.

372 Backscatter (and background) photons from M laser pulses are accumulated in

373 a single exposure of (e.g.) a CCD or CMOS frame by triggering the intensified

374 cameras' gate M times before finishing the exposure and reading the frame.
 375 There would be one exposure for each depth.

$$N_A = M \frac{E_p}{hc/\lambda} \eta_t \eta_r T_a^2 T_s^2 \exp(-2K_d z) \beta_{sw} \frac{1}{\delta_{sw} + 1} \frac{A}{(n_{sw} L + z)^2} \Delta z \quad (14)$$

$$N_B = M \frac{1}{2} \frac{L_{e,\Omega,\lambda}}{hc/\lambda} \eta_r \pi \left(FOV \frac{L}{2} \right)^2 \frac{A}{L^2} \frac{2\Delta z}{c/n_{sw}} \quad (15)$$

376 The delay of the intensified camera gate relative to the emission of the laser
 377 pulse is varied to sequentially probe each range bin. The gate width will be
 378 assumed to be fixed at 9 ns, which will provide a depth resolution of 1 m. Gate
 379 widths of <2 ns are possible with some cameras. The number of laser shots
 380 accumulated at a particular depth will vary exponentially with depth such that
 381 the SNR is mostly constant, with exponentially more shots required at greater
 382 depths. By this scheme, the overall time it takes for a gated, intensified camera
 383 with a maximum frame rate R_F to acquire N interferograms throughout a profile
 384 covering 0 to z_0 depth, with the number of shots increasing exponentially with
 385 depth according to the expected diffuse attenuation (K_d') until reaching a
 386 maximum of t_0 at the deepest point z_0 , will then be

$$\begin{aligned} \frac{N}{R_F} + t_0 \sum_{i=1}^N \exp(-2K_d' z_0 (i-1)/N) \\ = \frac{N}{R_F} + t_0 \frac{1 - \exp(-2K_d' z_0)}{1 - \exp(-2K_d' z_0/N)} \end{aligned} \quad (16)$$

387 Assume 1 s (4,000 shots) of accumulation at the deepest point and a camera
388 frame rate of 15 Hz. The time it takes to acquire a profile of 1 m resolution
389 through a column extending to 30 m depth is then 7.5 s, over which time the
390 aircraft, flying at 130 m/s, has traversed 975 m horizontally. For a K_d' of 0.3
391 /m and the same depth resolution (1 m), a profile extending 3 optical depths
392 takes 2.9 s to acquire while the aircraft traverses 374 m horizontally. Table 6
393 shows the expected number of backscattered and solar background photons, the
394 SNR in day and night, and the corresponding uncertainties in temperature,
395 salinity, and sound velocity at 30 m depth with 1 m resolution. The SNR and
396 background parameters come from Eq. (A 8) and Eq. (A 9), respectively. The
397 sensitivity is based on a temperature of 15 °C and salinity of 35 ppt. The
398 variance contributed by the dark noise and readout noise of the intensified
399 camera is assumed to be negligible compared to that contributed by shot noise
400 from backscatter.

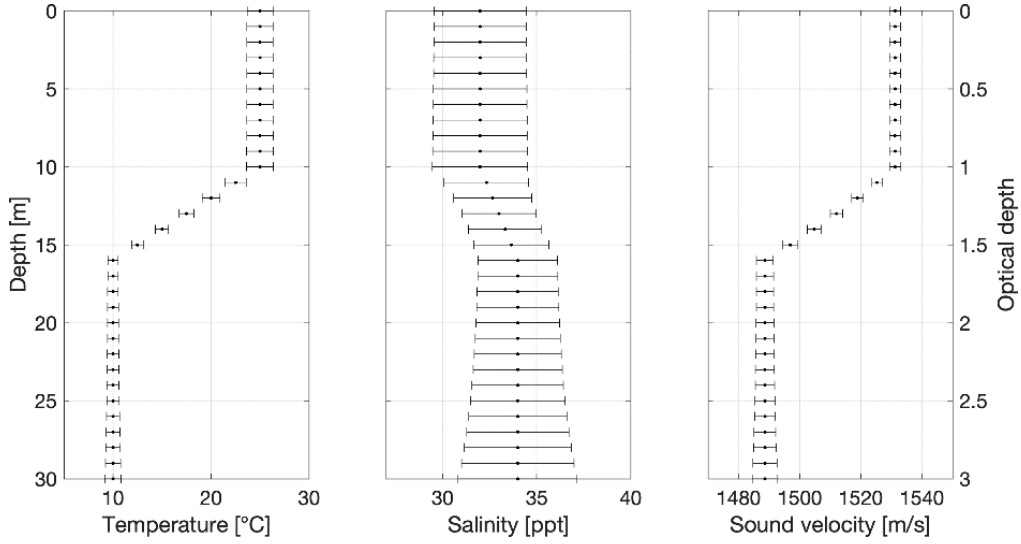
401 **Table 6. Cumulative backscatter and background photon number,**
402 **corresponding SNR, background parameter, and temperature, salinity,**
403 **and sound velocity 1σ random error for day (left column) and night**
404 **(right column) operation. These correspond to a 1 m bin at 30 m depth**
405 **with 1 second of averaging (4,000 shots) in water with a diffuse**
406 **attenuation of 0.1 /m.**

	Daytime	Nighttime
N_A	385,000	
N_B	441,000	0
SNR	186	272
F_B	0.07	-1
$\Delta T (1-\sigma)$	1.05 °C	0.67 °C
$\Delta S (1-\sigma)$	2.97 ppt	1.95 ppt
$\Delta V_s (1-\sigma)$	3.36 m/s	2.23 m/s

407

408 For the 3 cm OPD range and 6 cm OPD offset specified for this design, the
409 random errors in temperature are larger than those shown in Table 6 for warmer
410 waters. However, dense cooler waters will typically exist below warmer waters
411 and so cooler waters shall, in general, be more SNR starved than warmer waters
412 and therefore demand a higher sensitivity if measurement of temperature is the
413 objective. Conversely, for sound velocity, the warmer waters produce lower
414 uncertainties for this design. Other choices of OPD range and offset may
415 therefore be more optimal, depending on the target application. Fig. 5 shows a
416 profile of daytime retrievals of temperature, salinity, and sound velocity and
417 associated 1σ random errors for a temperature/salinity profile that is 25 °C/32
418 ppt from 0-10 m depth, descends linearly to 10 °C/34 ppt between 10-15 m

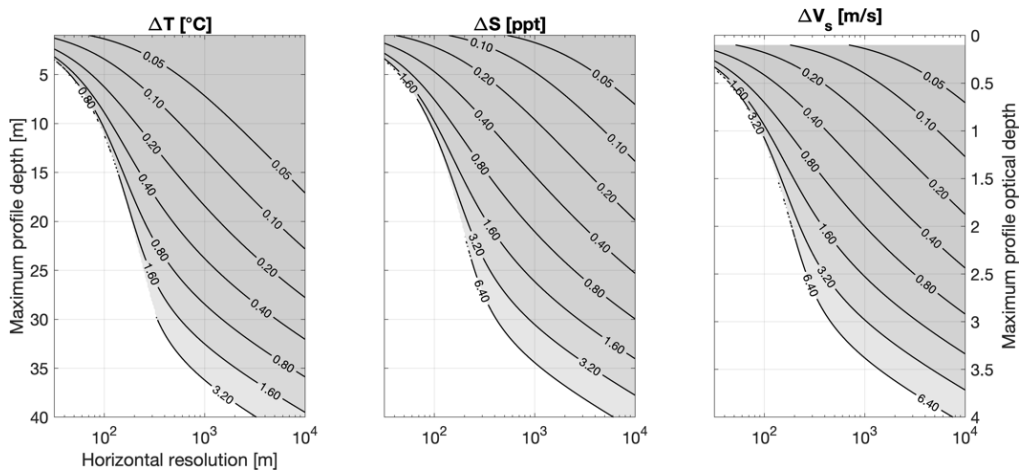
419 depth, and remains at that level from 15-30 m depth. The diffuse attenuation
 420 coefficient is 0.1 /m throughout, so an optical depth of three corresponds to 30
 421 m. This profile is meant to be representative of a sounding through a cold pool
 422 [31].



423
 424 Fig. 5. Retrieved temperature, salinity, and sound velocity with
 425 error bars showing 1σ random errors for optical depths of up to
 426 three during daytime. The physical depth resolution is 1 m and
 427 horizontal resolution is 1 km for this 0-30 m profile.

428 Using the camera gating scheme outlined above, the SNR is approximately
 429 constant throughout the column. The larger uncertainties in temperature and
 430 salinity at shallower depths in Fig. 5 are therefore due to the lower sensitivities
 431 to those quantities at higher temperatures. Fig. 5 shows that the gradient in
 432 temperature and sound velocity would be easily resolved, but not the salinity
 433 gradient.

434 For some applications, less depth penetration in exchange for finer
 435 horizontal resolution is preferable. For example, salinity profiles extending just
 436 one optical depth (or less) would be useful for mapping freshwater lenses and
 437 outflows. Temperature profiles extending two optical depths would be
 438 sufficient for profiling the active mixing layer across most of the ocean and
 439 determining the intensity, location and size of eddies and ocean fronts. These
 440 applications require a horizontal resolution sufficient to capture submesoscale
 441 feature lengths (~ 100 's m). With these objectives in mind, Fig. 6 shows the
 442 daytime random errors in temperature, salinity, and sound velocity across
 443 horizontal resolution and maximum profile depth. A fixed temperature/salinity
 444 of $15^\circ\text{C}/35$ ppt is assumed, along with a depth resolution of 1 m and 0.1 /m
 445 apparent attenuation.



446
 447 Fig. 6. A mapping of daytime random errors in temperature,
 448 salinity, and sound velocity for different horizontal averaging
 449 scales and maximum profile depths (i.e., deepest extent of the

450 profile). Contours are truncated where the number of shots at
451 the surface would be <1 .

452 **6. Systematic errors in temperature, salinity, and sound velocity**

453 Major sources of systematic error will be knowledge of the visibility factors,
454 knowledge of the Littrow heterodyne period, knowledge of solar background,
455 knowledge of gain ratio, knowledge of the linearity of the intensified camera,
456 and any variations in the spectral transmittance of the elastic scatter suppression
457 filter that might alter the apparent, relative strengths of the two Brillouin
458 doublet peaks (“Brillouin doublet imbalance”). The sensitivities of the
459 measurements of temperature, salinity, and sound velocity to each of these
460 factors are now investigated. This is done by performing a retrieval against a
461 “truth” temperature, salinity, and sound velocity and then introducing small
462 perturbations in the retrieval parameters to observe their effect on the retrieval,
463 which is essentially the same process as the Monte Carlo method outlined
464 earlier but with the random errors from detection noise replaced with systematic
465 errors in the retrieval inputs. The temperature is 15 °C, salinity is 35 ppt, solar
466 background is equal to backscatter ($F_B = 0$), gain ratio is assumed to be unity,
467 and the two visibility factors are assumed to be 0.8. The sensitivities are shown
468 in Table 7.

469 **Table 7. First order propagation of systematic errors in visibility factors,**
470 **Littrow heterodyne phase, solar background, gain ratio and Brillouin**

471 **doublet imbalance to errors in temperature, salinity, and sound velocity.**

472 **Values are the errors in T , S , or V_s per percent or radian error in the**

473 **parameter indicated in left column.**

	ΔT ($^{\circ}\text{C}$)	ΔS (ppt)	ΔV_s (m/s)
Visibility factor	-0.34 /%	0.74 /%	-0.21 /%
Littrow heterodyne phase	0.81 /rad	-1.03 /rad	1.35 /rad
Solar background	0.37 /%	-0.78 /%	0.25 /%
Gain ratio	-0.049 /%	-0.048 /%	-0.21 /%
Intensified camera linearity	0.016 /%	-0.030 /%	0.015 /%
Brillouin doublet imbalance	0.002 /%	0.005 /%	0.011 /%

474

475 For retrievals at the shallowest depths (<5 m), or during nighttime, the solar
476 background error sensitivity becomes negligible, but the linearity error
477 sensitivity amplifies to -0.21 $^{\circ}\text{C}/\%$ in temperature, 0.46 ppt/ $\%$ in salinity and -
478 0.12 m/s/ $\%$ in sound velocity and becomes the dominant error source. Both the
479 Littrow heterodyne phase and gain ratio can be assessed frequently and are
480 expected to be stable on profile acquisition timescales (~ 10 s). A phase error on
481 the order of a few mrad and gain ratio error of 1% is probably achievable,
482 making these error contributions to temperature and salinity negligible. The
483 gain ratio error is still significant to the sound velocity, however. The linearity

484 error could be made small by characterizing the camera's response. By Table
485 7, the sensitivity to error from Brillouin doublet imbalance is very small.
486 Therefore, the major sources of error in temperature and salinity are likely to
487 be the knowledge of the visibility factors and, for daytime operation and
488 retrievals from depth, knowledge of the solar background. The solar
489 background would need to be measured continually on a separate detector that
490 is episodically cross calibrated with the intensified camera. If we assume 1%
491 errors in the visibility factors, solar background and gain ratio, the root sum of
492 square errors in temperature, salinity, and sound velocity are 0.5 °C, 1.1 ppt,
493 and 0.4 m/s, respectively. Accurate knowledge of the visibility factors and solar
494 background will be more critical for warmer waters because the temperature
495 sensitivity of the Brillouin linewidth is significantly lower at warmer
496 temperatures. At 25 °C, the sensitivity to visibility factor error ~doubles to
497 about -0.8 °C/%, 1.5 ppt/% and -0.4 m/s/% and the sensitivity to solar
498 background error also ~doubles to 0.9 °C/%, -1.6 ppt/% and 0.5 m/s/% with
499 respect to the 15 °C case. A version of the retrieval of temperature that uses
500 only the Brillouin shift parameter – with assumption about salinity and errors
501 associated with that assumption – might therefore be more accurate for warmer
502 waters. An error of about 0.4 °C/ppt can be expected under this assumption
503 [32]. Substantially smaller errors in gradient measurements can be expected.
504 Also, absolute errors will be smaller if measurements can be periodically
505 “pinned” to coincident, collocated measurements from *in-situ*, microwave/IR

506 derived sea surface temperature (SST), microwave derived sea surface salinity
507 (SSS), or other sources.

508 Another potential source of systematic error is the effect of multiple scatter
509 on the backscatter spectrum. Simulations [33] have shown minimal corruption
510 of the Brillouin backscatter spectrum by multiple scatter, reasoning that since
511 particulates predominantly forward scatter that a direct backscatter by the
512 Brillouin process was significantly more probable than scatter at any other
513 angle for productive waters. For a purely Brillouin scattering water body more
514 corruption was noted, but this scattering regime is not seen in natural water
515 bodies, even in the open ocean. The effect of multiple scatter could be modeled
516 and quantified, but efforts to accurately model multiple scatter are often
517 confounded by inaccurate knowledge of the particulate scatter phase
518 function(s) for a particular water body. Other potential sources of error could
519 be inexact knowledge of the bulk and shear viscosities as a function of
520 temperature and salinity, so these might need to be verified in a water tank
521 demonstration, or the measurements episodically pinned to other temperature
522 and salinity data sources.

523 **7. Conclusions and science outlook**

524 An airborne Brillouin lidar capable of scientifically and operationally
525 meaningful remote sensing measurements of temperature, salinity, and sound
526 velocity is practical with current technology. The concept presented here

527 achieves an expected daytime (nighttime) random error of 1.1 °C (0.7 °C) in
528 temperature, 3.0 ppt (2.0 ppt) in salinity, and 3.4 m/s (2.2 m/s) in sound velocity
529 throughout a column that extends three optical depths with a depth resolution
530 of 1 m and horizontal resolution of 1 km. Similar performance is obtained for
531 profiles extending two (one) optical depths with a horizontal resolution of 200
532 m (100 m). The main sources of systematic error are the errors in knowledge of
533 the visibility factors and solar background, which might need to be known to
534 the sub-percent level for warmer waters, depending on requirements. Error in
535 the knowledge of the visibility factor, like other errors, would depend on the
536 accuracy with which the visibility factors can be assessed, combined with the
537 rate of these assessments and the rate of change between assessments. This and
538 the camera characterization would need to be part of a future study. More
539 advanced laser and detector technologies on the horizon could significantly
540 enhance performance beyond that shown here. A laser transmitter that emits in
541 the blue (470-490 nm) would offer twice the penetration depth in less
542 productive waters typical of the open ocean. Projects focused on the
543 development of blue laser transmitter technology are currently active in the US
544 and elsewhere. A large array of single photon sensitive elements (e.g., single
545 photon avalanche diodes) with integrated electronics that allow timing all
546 photons received from throughout the column would improve the horizontal
547 resolution of profiles extending three optical depths from 1 km to ~100 m and

548 the lower excess noise factor could afford a factor of ~ 1.6 reduction in random
549 error relative to existing intensified cameras. Such arrays are also being studied.

550 The Brillouin lidar receiver described herein would require a single mode
551 laser transmitter that is frequency stable and perhaps also frequency agile to a
552 limited degree. Workhorse airborne lidars with such transmitters and receivers
553 of similar size and complexity are deployed routinely by NASA [11-14, 29], so
554 a Brillouin lidar system based on this BASH spectrometer receiver concept
555 would be compact and lightweight enough to fly economically on one of
556 NASA's smaller aircraft, e.g., de Havilland Canada DHC-6 Twin Otter,
557 Beechcraft B200 King Air, or suitable unpiloted aerial vehicle (UAS) for near
558 shore operations as well as large aircraft for distant or longer duration
559 operations. The depth to which measurements can be made is limited to a few
560 10's of meters, piling in comparison to the depths possible with moorings,
561 floats, and ship-based sensors. However, an airborne sensor has unique
562 advantages in terms of deployment flexibility and spatial coverage. Such a lidar
563 could be quickly targeted to remote domains of specific interest by flying in a
564 fuel-efficient mode at cruise altitude and then acquiring low altitude
565 measurements over hundreds to thousands of kilometers at a sampling density
566 of the order 1 /km or better, providing synoptic scale transects containing
567 hundreds to thousands of profiles of temperature and salinity in a matter of
568 hours and at much lower cost than soundings from a ship or airborne
569 expendable bathythermographs and conductivity-temperature-depth (CTD)

570 probes. Such a lidar could complement *in-situ* sensors by improving their
571 targeting and providing a means for cross calibration. A lidar sensor would also
572 not suffer the thermal lag problem experienced with CTD sensors due to the
573 thermal mass of the sensor. The absence of thermal lag errors would have
574 significant advantages in resolving the depth of layers that have a steep gradient
575 in temperature, like cold pools [34, 35].

576 There are many potential science applications for an airborne Brillouin lidar.
577 Profiles from a lidar based on the BASH technique would provide valuable
578 information on mixed layer depth and the location, size, and intensity of eddies,
579 ocean fronts, cold pools, freshwater lenses, and freshwater outflows, and could
580 be used to study the fate of meltwater from sea ice and glaciers at high latitudes,
581 and its influence on upper ocean stratification and phytoplankton blooms [36].
582 Moreover, it would be straightforward to add simultaneous measurement of
583 particulate backscatter, which can be used to estimate phytoplankton biomass
584 and investigate phenomenon like diel vertical migration of zooplankton and
585 other marine animals. There are many potential science applications for an
586 airborne Brillouin lidar.

587 As a specific application, consider measurements of the position of the Mid-
588 Atlantic Bight (MAB) Cold Pool, which is spatiotemporally variable [37] and
589 is of prime importance for understanding the path and evolution of approaching
590 storms, especially tropical cyclones [38], and for predicting the movement of
591 fish species [39]. Mixing by tropical cyclones of the abundant cold bottom

592 water in the MAB with warmer surface water is known to be capable of causing
593 rapid deintensification, as in the case of Hurricane Irene (2011) prior to its New
594 Jersey landfall as an example [40]. In contrast, Hurricane Sandy (2012) was
595 able to cause immense destruction across New Jersey and New York because
596 of the disappearance of the Cold Pool off the coast that season [41], which
597 usually serves as a barrier to such storms. Model assimilation of rapidly
598 acquired temperature profiles across tropical cyclone tracks could therefore
599 improve forecasts and prevent excessively early or unnecessary evacuations.
600 For major population centers, reducing decision lead times from 72 to 48 hours
601 could save hundreds of millions of dollars in evacuation costs annually [42].
602 The MAB Cold Pool is warming and shrinking [43], speaking to the need for
603 more observations to track its evolution. There is also interest in understanding
604 the impact of offshore wind farm pylons on stratification of the MAB Cold Pool
605 [44], and implications for storms and fisheries. A temperature profiling lidar
606 could perform raster maneuvers around offshore wind farms to address this
607 observational need. Assimilation of lidar measured temperature profiles could
608 improve the skill of circulation models developed for the MAB and Gulf of
609 Maine that currently only assimilate data from satellite SST and *in-situ* sources
610 [45]. Root-mean-square errors of 0.86-4.64 °C were observed between
611 Saildrone and SST data [46], with the greater errors near the coast in summer
612 where (and when) reliable temperature data is most critical for storm
613 forecasting, compared with errors of 0.5 °C for the BASH. The value of the

614 BASH technique for forecasts of hurricane trajectory and intensification to the
615 open ocean. Hurricane trajectory models would benefit from assimilation of
616 temperature and salinity profiles from lidars installed on long-range, long-
617 duration Hurricane Hunter aircraft, e.g., NOAA's Lockheed WP-3D Orion fleet
618 and the Air Force Reserve's Lockheed-Martin WC-130J fleet, to fill gaps
619 between bathythermographs and CTD probes.

620 Another application of data from such a lidar would be improvement to
621 forecast models for red tide algal bloom events, e.g., off the West Florida
622 Continental Shelf [47]. Such blooms can evolve rapidly, and forecasts would
623 benefit from assimilation of temperature and salinity observations from an
624 airborne lidar to sensitive regions, and to improve targeting of *in-situ* assets.
625 General benefits of this temperature/salinity technique for many applications
626 include the ability for rapid targeted deployment and the ability to make
627 observations below clouds that thwart satellite SST retrievals. This lidar, if
628 developed, could have significant societal benefits for the US Atlantic and Gulf
629 Coast regions, and perhaps other regions with similar climates, e.g., the Indian
630 Ocean and Pacific Ocean typhoon basins.

631 Most of the applications above relate to temperature measurement, but there
632 is also significant interest in near-surface measurements of salinity. Microwave
633 (L-band) SSS instruments struggle to resolve submesoscale feature lengths,
634 even from aircraft. Also, in contrast with the Brillouin techniques, L-band SSS
635 retrievals are more challenged in cooler Arctic or near polar waters. A Brillouin

636 lidar could provide unprecedented horizontal resolution of near-surface salinity
 637 in these regions. Such measurements would therefore be well suited to studying
 638 inflows into the ocean from ice shelf melting that existing remote sensing
 639 instruments do not resolve well. A Brillouin lidar could also be well suited to
 640 studying freshwater lenses, which are shallow layers of freshwater above
 641 saltwater where gradients from 1 ppt to 25 ppt are often seen, and these layers
 642 exert strong control over refreezing. River outflows and plumes could be
 643 mapped to much higher spatiotemporal resolution than is possible with
 644 satellites, which only achieve resolutions of 0.25° (~ 30 km) in a 2-week period.
 645 Reasonable info exists on large rivers like the Amazon, but scant information
 646 exists on small rivers that are challenging to observe from space. Brillouin
 647 lidars could inform coastal hydrology and the fate of freshwater in river plumes,
 648 measure freshwater inputs from rainfall associated with strong convective
 649 storms in the inter-tropical convergence zone (ITCZ) and examine freshwater
 650 inputs at the ocean surface and the impacts of air-sea fluxes, i.e., heat fluxes. A
 651 Brillouin lidar could therefore help provide valuable insight into the climate
 652 and societal impacts of the exchange of freshwater and heat with the ocean.

653 **Appendix A: Variance of the normalized interferogram**

654 For simplification, assume that coefficients a_1 and a_2 are unity, that the
 655 visibility factors are equal ($M_1 = M_2 = M_i$) and that the detection efficiencies
 656 are also equal ($\eta_1 = \eta_2 = \eta$). Consider a two-dimensional image of the

657 normalized interferogram that is summed along the isophase lines of the
 658 Littrow heterodyne fringes (row-wise in Fig. 3) and in which i indexes through
 659 each of these P summations.

$$Q'_i = \frac{I_{1,i} - I_{2,i}}{I_{1,i} + I_{2,i}} = M_i Q_i \quad (\text{A } 1)$$

660 Q'_i is the normalized interferogram before correcting for the visibility factor
 661 and Q_i is consistent with its definition in Eq. (8). $I_{1,i}$ and $I_{2,i}$ are shorthand for
 662 $I_1(\delta_i)$ and $I_2(\delta_i)$, respectively, with

$$\delta_i = \Delta\delta \frac{(i-1)}{P} + \delta_0, \quad i = 1 \dots P \quad (\text{A } 2)$$

663 The variance of the ratio at each index i is approximately

$$\begin{aligned} \frac{\text{var } Q'_i}{Q_i'^2} &= \frac{\text{var}(I_{1,i} - I_{2,i})}{(\overline{I_{1,i}} - \overline{I_{2,i}})^2} + \frac{\text{var}(I_{1,i} + I_{2,i})}{(\overline{I_{1,i}} + \overline{I_{2,i}})^2} \\ &\quad - 2 \frac{\text{cov}(I_{1,i} - I_{2,i}, I_{1,i} + I_{2,i})}{(\overline{I_{1,i}} - \overline{I_{2,i}})(\overline{I_{1,i}} + \overline{I_{2,i}})} \end{aligned} \quad (\text{A } 3)$$

664 Where ‘var’ indicates variance and ‘cov’ indicates covariance. If the noises
 665 on $I_{1,i}$ and $I_{2,i}$ are uncorrelated detection noises, we have

$$\text{var}(I_{1,i} - I_{2,i}) = \text{var}(I_{1,i} + I_{2,i}) = \text{var } I_{1,i} + \text{var } I_{2,i} \quad (\text{A } 4)$$

$$\text{cov}(I_{1,i} - I_{2,i}, I_{1,i} + I_{2,i}) = \text{var } I_{1,i} - \text{var } I_{2,i} \quad (\text{A } 5)$$

666 The variance of the ratio is then

$$\text{var } Q'_i = \left(1 + \overline{Q'_i}^2\right) \frac{\text{var } I_{1,i} + \text{var } I_{2,i}}{(\overline{I_{1,i}} + \overline{I_{2,i}})^2} - 2\overline{Q'_i} \frac{\text{var } I_{1,i} - \text{var } I_{2,i}}{(\overline{I_{1,i}} + \overline{I_{2,i}})^2} \quad (\text{A } 6)$$

667 Define $\overline{N_{A,i}}$ and $\overline{N_{B,i}}$ as the mean number of total backscatter and background
 668 photons, respectively, accumulated at index i . If it is assumed that the detection
 669 of the signal plus background is shot noise and excess noise limited, then var
 670 $I_{1,i} + \text{var } I_{2,i} = \eta F (\overline{N_{A,i}} + \overline{N_{B,i}})$ and $\text{var } I_{1,i} - \text{var } I_{2,i} = \eta F \overline{Q'_i} \cdot \overline{N_{A,i}}$, with F
 671 being the excess noise factor of the intensified camera expressed in power
 672 (variance) space. The substitutions $\overline{Q'_i} \rightarrow M_i \overline{Q_i}$ and $\text{var } Q'_i \rightarrow M_i^2 \text{var } Q_i$ are now
 673 made. The variance of Q_i in terms of its expected value ($\overline{Q_i}$) is then given by
 674 Eq. (A 7).

$$\text{var } Q_i = \frac{1 + F_{B,i} M_i^2 \overline{Q_i}^2}{M_i^2 \text{SNR}_i^2} \quad (\text{A } 7)$$

675 Where SNR_i represents the signal-to-noise ratio of the sum of the signal in
 676 corresponding pixels of each interferogram at index i

$$\text{SNR}_i = \frac{\sqrt{\eta \overline{N_{A,i}}}}{\sqrt{F(1 + \overline{N_{B,i}}/\overline{N_{A,i}})}} \quad (\text{A } 8)$$

677 And $F_{B,i}$ is defined as the “background factor”

$$F_{B,i} = \frac{\overline{N_{B,i}} - \overline{N_{A,i}}}{\overline{N_{B,i}} + \overline{N_{A,i}}} \quad (\text{A } 9)$$

678 The background factor varies between -1 and $+1$, depending on the
 679 background relative to the backscatter in that pixel. If both the backscatter and
 680 background are uniformly distributed among P pixels, then $\text{SNR}_i^2 = \text{SNR}^2/P$

681 and $F_{B,i} = F_B$ and the variance of the normalized interferogram at each pixel
 682 becomes.

$$\text{var } Q_i = \frac{1 + F_B M_i^2 \bar{Q}_i^2}{M_i^2 \text{SNR}^2 / P} \quad (\text{A } 10)$$

683 **Appendix B: Propagation to variance and covariance in Brillouin**
 684 **shift and Brillouin linewidth**

685 Assume a least-squares fit of a model is applied to the normalized interferogram
 686 to retrieve the Brillouin shift, Brillouin linewidth and elastic scatter ratio. Since
 687 the variance of the normalized interferogram at each pixel is known by Eq. (A
 688 10), the uncertainties in the least squares fitting parameters can be estimated.
 689 To estimate these uncertainties, the covariance matrix (C) for the fitted
 690 parameters can be computed using the weighted Jacobian, J . The diagonal of
 691 the covariance matrix will contain the variances of the parameters.

$$C = (J^T J)^{-1} \quad (\text{B } 1)$$

692 The weighted Jacobian can be written as follows

$$J = \begin{pmatrix} \frac{\partial Q_1 / \partial v_B}{\sqrt{\text{var } Q_1}} & \frac{\partial Q_1 / \partial \Gamma_B}{\sqrt{\text{var } Q_1}} & \frac{\partial Q_1 / \partial \gamma}{\sqrt{\text{var } Q_1}} \\ \vdots & \vdots & \vdots \\ \frac{\partial Q_P / \partial v_B}{\sqrt{\text{var } Q_P}} & \frac{\partial Q_P / \partial \Gamma_B}{\sqrt{\text{var } Q_P}} & \frac{\partial Q_P / \partial \gamma}{\sqrt{\text{var } Q_P}} \end{pmatrix} \quad (\text{B } 2)$$

693 With $\text{var } Q_i$ given by Eq. (A 10) and

$$\begin{aligned} & \partial Q_i / \partial v_B \\ &= -2\pi \frac{\delta_i}{c} \frac{1}{1+\gamma} \exp\left(-\frac{\pi \Gamma_B \delta_i}{c}\right) \sin\left(\frac{2\pi v_B \delta_i}{c}\right) \cos\left(\frac{2\pi(v_L - v_0)\delta_i}{c}\right) \end{aligned} \quad (\text{B } 3)$$

$$\begin{aligned} & \partial Q_i / \partial \Gamma_B \\ &= -\pi \frac{\delta_i}{c} \frac{1}{1+\gamma} \exp\left(-\frac{\pi \Gamma_B \delta_i}{c}\right) \cos\left(\frac{2\pi v_B \delta_i}{c}\right) \cos\left(\frac{2\pi(v_L - v_0)\delta_i}{c}\right) \end{aligned} \quad (\text{B } 4)$$

$$\begin{aligned} & \partial Q_i / \partial \gamma \\ &= \frac{1}{(1+\gamma)^2} \left(1 \right. \\ & \quad \left. - \exp\left(-\frac{\pi \Gamma_B \delta_i}{c}\right) \cos\left(\frac{2\pi v_B \delta_i}{c}\right) \right) \cos\left(\frac{2\pi(v_L - v_0)\delta_i}{c}\right) \end{aligned} \quad (\text{B } 5)$$

694 δ_i is defined in (A 2). After solving the covariance matrix, the variances in
 695 Brillouin shift and linewidth are along the diagonal and the covariance is in the
 696 off-diagonal.

$$C = \begin{pmatrix} \Delta v_B^2 & \Delta v_B \Delta \Gamma_B \\ \Delta v_B \Delta \Gamma_B & \Delta \Gamma_B^2 \end{pmatrix} \quad (\text{B } 6)$$

697 The third row and column contain the covariance of the elastic scatter ratio,
 698 but this parameter has no relationship to temperature and salinity and so is
 699 omitted from (B 6) and ignored going forward.

700 **Appendix C: Propagation to variance in temperature, salinity, and**
 701 **sound velocity**

702 Once the Brillouin linewidth and Brillouin shift are measured, the temperature
 703 and salinity can be retrieved using an iterative process. Starting with an initial
 704 guess and the measured Brillouin shift and linewidth, the temperature and
 705 salinity are solved using the Gauss-Newton algorithm, implemented by
 706 iterating on Eq. (C 1). $T_{k=0}$ and $S_{k=0}$ are the initial guesses and ν'_B and Γ'_B are
 707 the measured Brillouin shift and Brillouin linewidth.

$$\begin{pmatrix} T_{k+1} \\ S_{k+1} \end{pmatrix} = \begin{pmatrix} T_k \\ S_k \end{pmatrix} + J'^{-1} \cdot \left[\begin{pmatrix} \nu'_B \\ \Gamma'_B \end{pmatrix} - \begin{pmatrix} \nu_B(T_k, S_k) \\ \Gamma_B(T_k, S_k) \end{pmatrix} \right] \quad (\text{C } 1)$$

708 J' is a new Jacobian describing the sensitivities of the Brillouin shift and
 709 linewidth to temperature and salinity.

$$J' = \begin{pmatrix} \partial \nu_B(T_k, S_k) / \partial T & \partial \nu_B(T_k, S_k) / \partial S \\ \partial \Gamma_B(T_k, S_k) / \partial T & \partial \Gamma_B(T_k, S_k) / \partial S \end{pmatrix} \quad (\text{C } 2)$$

710 To determine the covariance in temperature and salinity, the Brillouin shift
 711 and linewidth covariance matrix from Eq. (B 6) is transformed into a covariance
 712 in temperature and salinity (C') using Jacobian J' .

$$C' = J'^{-1} C (J'^{-1})^T \quad (\text{C } 3)$$

713 After solving the covariance matrix, the variances in temperature and
 714 salinity are along the diagonal and the covariance is in the off-diagonal.

$$C' = \begin{pmatrix} \Delta T^2 & \Delta T \Delta S \\ \Delta T \Delta S & \Delta S^2 \end{pmatrix} \quad (\text{C } 4)$$

715 The temperature and salinity covariance matrix can be converted to a
716 random error in sound velocity using its sensitivities to those variables, by
717 analogy with Eq. (C 3).

$$(\Delta V_s)^2 = (\partial V_s / \partial T \quad \partial V_s / \partial S) C' \begin{pmatrix} \partial V_s / \partial T \\ \partial V_s / \partial S \end{pmatrix} \quad (C 5)$$

718

719 **Funding.** NASA Earth Science Technology Office (80NSSC21M0021).

720 **Acknowledgements.** The author sincerely thanks John Hair and Brian

721 Collister for their valuable advice on ocean lidar and seawater optical

722 properties, Matt Oliver, Michael Behrenfeld, Peter Gaube and Emmanuel

723 Boss for valuable discussions on potential applications in oceanography

724 and John Harlander and Ian Miller for valuable discussions on the design

725 of the polarizing DASH interferometer.

726 **Disclosures.** The author declares no conflict of interest.

727 **Data availability.** No data were generated or analyzed in the presented

728 research.

729 **8. References**

- 730 1. A. Popescu, K. Schorstein, and T. Walther, "A novel approach to a
731 Brillouin–LIDAR for remote sensing of the ocean temperature," Appl.
732 Phys. B 79, 955-961 (2004).

- 733 2. G. Hickman, J. Harding, M. Carnes, *et al.*, "Aircraft laser sensing of
734 sound velocity in water: Brillouin scattering," *Remote Sens. of Environ.*
735 36 (3), 165-178 (1991).
- 736 3. K. Liang, Y. Ma, J. Huang, *et al.*, "Precise measurement of Brillouin
737 scattering spectrum in the ocean using F-P etalon and ICCD," *Applied*
738 *Physics B* 105, 421-425 (2011).
- 739 4. Y. Emery and E. Fry, "Laboratory development of a LIDAR for
740 measurement of sound velocity in the ocean using Brillouin scattering,"
741 *Ocean Optics XIII Vol. 2963*, SPIE (1997).
- 742 5. Y. Ma, Y. Yu, H. Li, *et al.*, "Accurate measurement of high resolution
743 spectrum obtained by F-P etalon and ICCD," *Appl. Phys. B* 116, 575-
744 584 (2014).
- 745 6. K. Schorstein, E. Fry and T. Walther, "Depth-resolved temperature
746 measurements of water using the Brillouin lidar technique," *Appl. Phys.*
747 *B* 97, 931-934 (2009).
- 748 7. R. Dai, W. Gong, J. Xu, *et al.*, "The edge technique as used in Brillouin
749 lidar for remote sensing of the ocean," *Appl. Phys. B* 79, 245-248 (2004).
- 750 8. C. Englert, J. Harlander, D. Babcock, *et al.*, "Doppler asymmetric spatial
751 heterodyne spectroscopy (DASH): an innovative concept for measuring
752 winds in planetary atmospheres," *Atmos. Opt. Modeling, Meas., and Sim.*
753 *II* 6303, SPIE (2006).

- 754 9. C. Englert, D. Babcock, and J. Harlander, "Doppler asymmetric spatial
755 heterodyne spectroscopy (DASH): concept and experimental
756 demonstration," *Appl. Opt.* 46 (29), 7297-7307 (2007).
- 757 10. C. Englert, C. Brown, K. Marr, *et al.*, "As-built Specifications of
758 MIGHTI–The Thermospheric Wind and Temperature Instrument for the
759 NASA ICON Mission," *Fourier Trans. Spect.* (2016).
- 760 11. S. Burton, C. Hostetler, A. Cook, *et al.*, "Calibration of a high spectral
761 resolution lidar using a Michelson interferometer, with data examples
762 from ORACLES," *Appl. Opt.* 57 (21), 6061-6075 (2018).
- 763 12. S. Burton, R. Ferrare, C. Hostetler, *et al.*, "Second Generation Airborne
764 High Spectral Resolution Lidar (HSRL-2) Measurements of Various
765 Types of Aerosols During ORACLES, CAMP2EX, and ACTIVATE,"
766 *Proc. AGU Fall Meeting*, 2021AGUFM.A15C1650B (2021).
- 767 13. P. Sawamura, R. Moore, S. Burton, *et al.*, "HSRL-2 aerosol optical
768 measurements and microphysical retrievals vs. airborne in situ
769 measurements during DISCOVER-AQ 2013: an intercomparison study,"
770 *Atmos. Chem. & Phys.* 17 (11), 7229-7243 (2017).
- 771 14. D. Müller, C. Hostetler, R. Ferrare, *et al.*, "Airborne Multiwavelength
772 High Spectral Resolution Lidar (HSRL-2) observations during TCAP
773 2012: vertical profiles of optical and microphysical properties of a
774 smoke/urban haze plume over the northeastern coast of the US," *Atmos.*
775 *Meas. Tech.* 7 (10), 3487-3496 (2014).

- 776 15. J. Harlander and C. Englert, "Design of a real-fringe DASH
777 interferometer for observations of thermospheric winds from a small
778 satellite," *Fourier Trans. Spect. FW1D.2* (2013).
- 779 16. X. Quan and E. Fry, "Empirical equation for the index of refraction of
780 seawater," *Appl. Opt.* 34 (18), 3477-3480 (1995).
- 781 17. N. Fofonoff, R. Millard Jr., "Algorithms for the computation of
782 fundamental properties of seawater," *UNESCO Technical Papers in*
783 *Marine Sciences* 44 (1983).
- 784 18. J. Xu, X. Ren, W. Gong, *et al.*, "Measurement of the bulk viscosity of
785 liquid by Brillouin scattering," *Appl. Opt.* 42 (33), 6704-6709 (2003).
- 786 19. M. Sharqawy, J. Lienhard, and S. Zubair, "Thermophysical properties of
787 seawater: a review of existing correlations and data," *Desalination &*
788 *Water Treatment* 16 (1-3), 354-380 (2010).
- 789 20. D. Bruneau and J. Pelon, "Simultaneous measurements of particle
790 backscattering and extinction coefficients and wind velocity by lidar with
791 a Mach-Zehnder interferometer: principle of operation and performance
792 assessment," *Appl. Opt.* 42 (6), 1101-1114 (2003).
- 793 21. J. Churnside, "Review of profiling oceanographic lidar," *Opt. Eng.* 53 (5),
794 051405 (2014).
- 795 22. J. Harlander, "Algebraic ray trace analysis of spatial heterodyne
796 spectrometers," *Appl. Opt.* 62 (16), 4288-4300 (2023).

- 797 23. D. Liu, J. Shi, X. Chen, *et al.*, "Brillouin lidar and related basic physics,"
798 Front. Phys. China 5, 82-106 (2010).
- 799 24. G. Scarcelli and S. Hyun Yun, "Multistage VIPA etalons for high-
800 extinction parallel Brillouin spectroscopy," Opt. Express 19 (11), 10913-
801 10922 (2011).
- 802 25. Z. Meng and V. Yakovlev, "Precise determination of Brillouin scattering
803 spectrum using a virtually imaged phase array (VIPA) spectrometer and
804 charge-coupled device (CCD) camera," Appl. Spect. 70 (8), 1356-1363
805 (2016).
- 806 26. Z. Coker, M. Troyanova-Wood, A. Traverso, *et al.*, "Assessing
807 performance of modern Brillouin spectrometers," Opt. Express 26 (3),
808 2400-2409 (2018).
- 809 27. C. Xie, P. Wang, C. Cai, *et al.*, "A Simple and accurate method for
810 Brillouin spectroscopy based on virtual imaging phased array
811 spectrometer and charge-coupled device cameras," Opt. Commun. 488,
812 126821 (2021).
- 813 28. I. Miller, LightMachinery, 80 Colonnade Road North, Unit #1, Ottawa,
814 ON K2E 7L2, Canada (personal communication, 2023).
- 815 29. J. Hair, C. Hostetler, Y. Hu, *et al.*, "Combined atmospheric and ocean
816 profiling from an airborne high spectral resolution lidar," EPJ Web of
817 Conferences 119 EDP Sciences (2016).

- 818 30. Y. Zhou, W. Chen, D. Liu, *et al.*, "Multiple scattering effects on the
819 return spectrum of oceanic high-spectral-resolution lidar," *Opt. Express*
820 27 (21), 30204-30216 (2019).
- 821 31. W. Brown, O. Schofield, S. Glenn, *et al.*, "Mid-Atlantic Bight cold pool
822 based on ocean glider observations," *Cont. Shelf Res.* 264, 105040
823 (2023).
- 824 32. E. Fry, Y. Emery, X. Quan, *et al.*, "Accuracy limitations on Brillouin
825 lidar measurements of temperature and sound speed in the ocean," *Appl.*
826 *Opt.* 36 (27), 6887-6894 (1997).
- 827 33. B. Joelson and G. Kattawar, "Multiple scattering effects on the remote
828 sensing of the speed of sound in the ocean by Brillouin scattering," *Appl.*
829 *Opt.* 35 (15), 2693-2701 (1996).
- 830 34. B. Garau, S. Ruiz, W. Zhang, *et al.*, "Thermal lag correction on Slocum
831 CTD glider data," *J. Atmos. Ocean. Technol.* 28 (9), 1065-1071 (2011).
- 832 35. Y. Wang, C. Luo, S. Yang, *et al.*, "Modified thermal lag correction of
833 CTD data from underwater gliders," *J. Coast. Res.* 99 (sp1), 137-143
834 (2020).
- 835 36. X. Lu, Y. Hu, Y. Yang, *et al.*, "Antarctic spring ice-edge blooms
836 observed from space by ICESat-2," *Remote Sens. Environ.* 245, 111827
837 (2020).

- 838 37. Z. Chen and E. Curchitser, "Interannual Variability of the Mid-Atlantic
839 Bight Cold Pool," J. Geophys. Res. Oceans 125 (8), e2020JC016445
840 (2020).
- 841 38. G. Seroka, T. Miles, Y. Xu, *et al.*, "Rapid shelf-wide cooling response of
842 a stratified coastal ocean to hurricanes," J. Geophys. Res. Oceans 122 (6),
843 4845-4867 (2017).
- 844 39. H. du Pontavice, T. Miller, B. Stock, *et al.*, "Ocean model-based
845 covariates improve a marine fish stock assessment when observations are
846 limited," ICES J. Mar. Sci. 79 (4), 1259-1273 (2022).
- 847 40. S. Glenn, T. Miles, G. Seroka, *et al.*, "Stratified coastal ocean interactions
848 with tropical cyclones," Nat. Commun. 7 (1), 10887 (2016).
- 849 41. T. Miles, S. Glenn, J. Kohut, *et al.*, "Observations of Hurricane Sandy
850 from a glider mounted aquadopp profiler," Proc. 2013 OCEANS-San
851 Diego IEEE (2013).
- 852 42. E. Regnier, "Public evacuation decisions and hurricane track
853 uncertainty," Manag. Sci. 54 (1), 16-28 (2008).
- 854 43. K. Friedland, T. Miles, A. Goode, *et al.*, "The Middle Atlantic Bight Cold
855 Pool is warming and shrinking: Indices from in situ autumn seafloor
856 temperatures," Fish. Oceanogr. 31 (2), 217-223 (2022).
- 857 44. T. Miles, S. Murphy, J. Kohut, *et al.*, "Offshore wind energy and the Mid-
858 Atlantic Cold Pool: A review of potential interactions," Mar. Technol.
859 Soc. J. 55 (4), 72-87 (2021).

- 860 45. A. López, J. Wilkin, and J. Levin, "Doppio—a ROMS (v3. 6)-based
861 circulation model for the Mid-Atlantic Bight and Gulf of Maine:
862 configuration and comparison to integrated coastal observing network
863 observations," *Geosci. Model Dev.* 13 (8), 3709-3729 (2020).
- 864 46. K. Koutantou, P. Brunner, and J. Vazquez-Cuervo, "Validation of NASA
865 Sea Surface Temperature Satellite Products Using Saildrone Data," *Rem.
866 Sens.* 15 (9), 2277 (2023).
- 867 47. R. Weisberg, A. Barth, A. Alvera-Azcárate, *et al.*, "A coordinated coastal
868 ocean observing and modeling system for the West Florida Continental
869 Shelf," *Harmful Algae* 8 (4), 585-597 (2009).